JGR Oceans

RESEARCH ARTICLE
10.1029/2024JC022064

Special Collection:
Forcing, response, and impacts of coastal storms in a changing climate

The Impacts of an Explosive Cyclone on the Upper Ocean and Sea Ice Over the Southern Ocean Based on Numerical Modeling Results

Xiaoqi Xu[1,2,3], Jiping Liu[4], Chao-Yuan Yang[5], Gang Huang[1,3], and Mirong Song[1]

[1]Key Laboratory of Earth System Numerical Modeling and Application, Institute of Atmospheric Physics, Chinese Academy of Sciences, Beijing, China, [2]Institute for Development and Programme Design, China Meteorological Administration, Beijing, China, [3]University of Chinese Academy of Sciences, Beijing, China, [4]School of Atmospheric Sciences, Sun Yat-sen University and Southern Marine Science and Engineering Guangdong Laboratory (Zhuhai), Zhuhai, China, [5]Southern Marine Science and Engineering Guangdong Laboratory (Zhuhai), Zhuhai, China

Abstract Explosive cyclones are intense extratropical synoptic systems associated with severe weather in the mid-to-high latitudes, particularly over the Southern Ocean. This study employs a recently developed ROMS-CICE coupled model, incorporating a cyclone-removal method, to simulate and quantify the response of the upper ocean and sea ice to an explosive cyclone traversing the Southern Pacific Ocean. The modeling results indicate that the maximum instantaneous sea surface warming anomaly reaches up to 0.20°C around the center of the explosive cyclone, while a cooling anomaly of about −0.15°C is observed at the cyclone's periphery. Beneath this surface anomaly, a cooling of up to −0.15°C occurs in the area-averaged subsurface ocean layer at depths of 20–60 m. Concurrently, the sea surface salinity experiences an increasing anomaly of up to 0.20 practical salinity units (psu), accompanied by a decrease in salinity within the subsurface ocean layer at depths of 30–60 m. These anomalies gradually weaken over the subsequent 28–30 days but sustain minor anomalies for more than 1 month, particularly in the subsurface ocean layer. Further analysis of the temperature and salinity tendency equations reveals that advection and vertical diffusion primarily contribute to both the surface and subsurface responses, with vertical diffusion serving as the main driver behind the observed uniform patterns. Additionally, sea ice concentration and thickness demonstrate reductions of more than 25% and 0.2 m near the coast, respectively, resulting from dynamic forcing and the contributions of basal ice melting due to the transport of warmer water currents beneath.

Plain Language Summary This study investigates how an explosive cyclone (strong storm system) over the Southern Ocean affects the upper ocean and sea ice. Using an advanced ocean-ice coupled model that removes cyclone influences in atmospheric fields, we found that the storm can create significant changes in upper ocean temperature and salinity. Near the cyclone's center, the ocean surface warms slightly, while it cools further out. Beneath the surface, the water cools even more at depths of 20–60 m. The storm also causes an increase in surface salinity and a slight drop in subsurface salinity at 30–60 m depth. These changes gradually weaken over about a month but remain noticeable, especially in deeper layers under 50 m. The study reveals that water movement and mixing are the main drivers of these temperature and salinity changes. Additionally, sea ice near the coast thins and decreases in concentration due to warmer water moving underneath, causing some melting. This result helps us understand how intense storms impact upper ocean and ice systems in the Southern Ocean.

Key Points:

- This study uses a newly developed ocean-ice model to quantify the impact of an explosive cyclone (EC) in the Southern Pacific Ocean
- EC causes upper ocean temperature and salinity anomalies, peaking at 20–60 m depth, mainly due to vertical diffusion
- EC leads to over 25% reduction in sea ice concentration and 0.2 m thickness decrease, driven by dynamic forcing and warm water influx

Supporting Information:

Supporting Information may be found in the online version of this article.

Correspondence to:

J. Liu,
liujp63@mail.sysu.edu.cn

Citation:

Xu, X., Liu, J., Yang, C.-Y., Huang, G., & Song, M. (2025). The impacts of an explosive cyclone on the upper ocean and sea ice over the southern ocean based on numerical modeling results. *Journal of Geophysical Research: Oceans*, *130*, e2024JC022064. https://doi.org/10.1029/2024JC022064

Received 2 NOV 2024
Accepted 13 JUN 2025

Author Contributions:

Conceptualization: Xiaoqi Xu, Jiping Liu
Investigation: Xiaoqi Xu
Methodology: Xiaoqi Xu, Chao-Yuan Yang
Software: Mirong Song
Supervision: Jiping Liu
Visualization: Xiaoqi Xu
Writing – original draft: Xiaoqi Xu
Writing – review & editing: Jiping Liu, Chao-Yuan Yang, Gang Huang, Mirong Song

1. Introduction

Explosive cyclones (ECs) are severe synoptic systems characterized by a rapid reduction in central pressure (at least 24 hPa in 24 hr), strong intensification, and longer duration compared to ordinary extratropical cyclones (Francis et al., 2021; Lim & Simmonds, 2002; Reale et al., 2019; Sanders & Gyakum, 1980). They usually occur in mid-to-high latitude ocean (Hoskins & Hodges, 2005; Schossler et al., 2018; Vichi et al., 2019), associated with meteorological hazards, including strong winds (Ashley & Black, 2008), heavy precipitation (Catto et al., 2015; Osbrough & Frederiksen, 2021; Pfahl & Wernli, 2012), coastal storm surges (Colle et al., 2008), sea ice removal (Francis et al., 2019, 2020), ice front calving (Francis et al., 2021, 2022) and ice shelf disintegration (Jena et al., 2022; Vichi et al., 2019). The Southern Ocean is home to ECs, most of them typically follow southeastward trajectories, undergoing net cyclogenesis in the mid-latitudes and net cyclolysis closer to the Antarctic continent

(Reale et al., 2019; Wille et al., 2024a, 2024b). With the application of automated cyclone tracking schemes and improved quality of atmospheric reanalysis data, analyses of ECs have become possible (Grieger et al., 2018; Lim & Simmonds, 2002; Neu et al., 2013; Sinclair, 1994, 1995). Some studies showed that the ECs in the Southern Hemisphere are observed to increase (Reale et al., 2019; Reboita et al., 2015; Xu et al., 2024) and this increasing trend is expected to continue in the future under global warming (Chang, 2017; Chang et al., 2012).

These severe synoptic systems are responsible for atmospheric circulation changes, enhancing exchange of heat and moisture at the air-sea interface and energy transport, modifying surface heat fluxes, ocean, and sea ice (Bengtsson et al., 2009; Lin et al., 2023). The regions of increased moisture flux south of 60°S in the Atlantic are related to the occurrence of strong cyclones (Grieger et al., 2018). It is estimated that about 60%–90% of the strong precipitation events in the Southern Ocean are due to synoptic systems (Papritz et al., 2014). When they pass over sea surface, they import kinetic energy into surface waves and currents, and then contribute to ocean diffusivity and circulation. The enhanced heat fluxes at air-sea interface change the regional ocean heat uptake and modulate sea surface temperature (Papritz et al., 2014; Vichi et al., 2019; Xu et al., 2022). At the circumpolar regions, strong winds associated with the cyclones generate large ocean waves and swells which propagate into the sea ice zone, breaking up the ice and leading to ice melt (Jena et al., 2022; Turner et al., 2020; Vichi et al., 2019).

Several studies have linked variability of high-latitude ocean and sea ice to synoptic cyclones events. Vichi et al. (2019) used in situ and ship-based observations to analyze an EC crossing the marginal ice zone in 2017. They showed that the EC contributes to the advection of warm, moist air southward in the open ocean, but the net ocean-atmosphere heat flux is supposedly balanced by the ocean heat gain in the warm sector and heat loss in the cold sector. When the extratropical cyclones move closer to the Antarctic continent, they often induce cold air outbreaks on the western side (Bracegirdle & Kolstad, 2010; Papritz et al., 2014; Vichi et al., 2019), which are expected to strongly affect heat fluxes closer to sea ice. Jena et al. (2022) used observational data to analyze the impacts of a series of intense and explosive polar cyclones over the Weddell Sea that forced an exceptional decline in sea ice extent during April–May 2019. The results showed that the largest anomalous net surface heat flux can reach 138 W/m^2, along with ocean mixed layer warming up to 2°C. Several works have also indicated that ECs maybe one of the drivers of the trend observed in Antarctic sea ice extent in recent years (Maksym, 2019; Schemm, 2018; Schlosser et al., 2018; Turner et al., 2020).

Although the study of ECs in the Southern Ocean continues, our understanding of their interactions with ocean and sea ice around Antarctica remains incomplete. The mechanism of upper ocean variability associated with the ECs is difficult to investigate when only using the reanalysis products, considering their uncertainty due to inadequate in situ observations being ingested into the data assimilation (Jena et al., 2022). Moreover, the background pressure field tends to be lower toward higher latitude regions, that means the effects of ECs derived from the observation and reanalysis data includes the contributions of non-synoptic scale systems. To distinguish the role of cyclone and background field, numerical simulations are required. A few studies of tropical cyclones have applied a cyclone removal technique to examine the Tropical Cyclone-induced changes of atmospheric environments during their evolution (Arakane & Hsu, 2020; Ross & Kurihara, 1995; Wang et al., 2015). In contrast, this approach has been less applied to high-latitude extratropical cyclones; only a few studies have been conducted in the high latitudes of the Northern Hemisphere. For example, Zhang et al. (2013) used the coupled Pan-Arctic Ice-Ocean Modeling and Assimilation System (PIOMAS) to simulate the impacts of an August 2012 storm event on Arctic sea ice and upper ocean conditions. Their analysis primarily focused on comparing sea ice conditions before and after the storm passage to quantify its effects.

As demonstrated in Xu et al. (2024), the southern Pacific Ocean sector is an important region for ECs generation and is accompanied with increasing trend in recent decades. According to the key region with the highest and most significant increasing trend of deepened ECs in autumn over the southern Pacific Ocean (155°W–170°W, 50°S–65°S; cf. Figure 5 in Xu et al., 2024), here we choose an EC generated and deepened in the key region over the southern Pacific Ocean from 24th to 30 April 2002 to quantify its impacts. We apply a cyclone-removal method and a recently developed ocean-ice coupled model to the EC event and conduct a pair of numerical experiments. The modeling results quantitatively assess the impacts and persistence of this EC on the upper ocean and sea ice. We also investigate the dominant physical processes for the changes of upper ocean and sea ice induced by this EC, to further our understanding of atmosphere-ocean-sea ice interactions.

2. Data and Methods

2.1. Data

The 6-hourly atmospheric data used in the cyclone detection algorithm and as atmospheric forcing field for the ocean-ice coupled model is obtained from the latest generation European Center for Medium-Range Weather Forecasts (ECMWF) reanalysis (ERA5; Hersbach et al., 2018, 2020), including mean sea level pressure, near surface air temperature and winds, sensible and latent heat fluxes, downward shortwave and longwave radiation, surface air relative humidity, total precipitation rate, snowfall rate, and total cloud cover with a spatial resolution of 0.25°. The ERA5 reanalysis is based on the global Numerical Weather Prediction Model Integrated Forecast System (IFS) Cy41r2, thus benefiting from a decade of developments in model physics, core dynamics and data assimilation. It shows an improved fit for temperature, wind and humidity in the troposphere when compared with radiosonde and pilot data prior to assimilation. The daily sea ice concentration data is from the National Snow and Ice Data Center (NSIDC) Climate Data Record of Passive Microwave Sea Ice Concentration (Version 4) with a spatial resolution of 25 km × 25 km (NSIDC CDR; Meier et al., 2021).

Initial and boundary conditions for ocean and ice in the ocean-ice coupled model are generated from the National Centers for Environmental Prediction (NCEP) Climate Forecast System Reanalysis (CFSR) with a horizontal resolution of 0.5° and vertical resolution of 40 levels. CFSR is superior to previous NCEP reanalysis with respect to improved model, higher resolution in time and space, advanced assimilation schemes, atmosphere-land-ocean-sea ice coupling, and assimilates satellite radiances rather than retrievals (Saha et al., 2014).

2.2. The Ocean-Ice Coupled Model

In this study, we use a recently developed ocean-ice coupled model configured for the Antarctic with sufficient flexibility (Yang et al., 2020; hereafter referred to as Y20). Specifically, we have coupled the Los Alamos sea ice model (referred to as Community Ice CodE; CICE version 6.0.0; Hunke et al., 2018) with the Regional Ocean Modeling System model (ROMS version 3.8; Shchepetkin & McWilliams, 2005, 2009) using the Model Coupling Toolkit in the Coupled Ocean-Atmosphere-Wave-Sediment Transport (COAWST) modeling system (Warner et al., 2010). The ROMS and CICE model have been widely used in a diverse range of applications (Bi et al., 2020; Bruneau & Toumi, 2016; Hunke et al., 2015; Kumar et al., 2021; Perelman et al., 2024; Rae et al., 2014; Yang et al., 2022).

The ROMS model is a free-surface, terrain-following model that primarily solves the three-dimensional Reynolds-averaged Navier-Stokes equations under the hydrostatic pressure and Boussinesq approximations (Haidvogel et al., 2008; Shchepetkin & McWilliams, 2005). Horizontally, ROMS employs a boundary-fitted orthogonal curvilinear coordinate system and discretizes the equations on a staggered Arakawa C-grid. Vertically, the governing equations are discretized based on bottom topography using a terrain-following stretched coordinate system (Song & Haidvogel, 1994). This S-coordinate system, originally developed by Haidvogel et al. (1991), offers high design flexibility. By incorporating non-uniform vertical layering and adjustable parameters, the S-coordinate can be transformed into traditional sigma coordinates, thereby enhancing grid resolution. For simulating ocean physical processes, ROMS provides multiple parameterization options, including advection schemes for momentum and tracers, vertical mixing schemes, subgrid-scale parameterizations, and open boundary conditions. Due to its flexible configuration and reliable performance, the ROMS ocean model has been widely applied in various marine science studies.

The CICE model consists of three main modules: dynamics, thermodynamics, and transport. Additionally, CICE introduces the innovative Ice Thickness Distribution (ITD) concept (Thorndike et al., 1975), enabling the simulation of spatiotemporal evolution of sea ice across different thickness categories. The model provides three different thickness distribution boundary classification schemes based on variations in sea ice thickness. The default setting is the "original" classification, which consists of 5 categories (plus open water). This configuration is generally sufficient to simulate the annual cycle of ice thickness, ice strength, and surface fluxes (see Bitz et al., 2001; Lipscomb, 2001). This feature is crucial for accurately characterizing the dynamic and thermodynamic properties of ice cover, as these properties depend heavily on the distribution of ice within each thickness range. For detailed technical descriptions and theoretical frameworks of the CICE model, refer to the official documentation by Hunke et al. (2015).

The basic configuration of ROMS and CICE are referred to as Y20, except the tracer advection scheme and vertical mixing scheme in ocean model. As suggested by Naughten et al. (2017), the upwind third-order advection scheme performs better than other advection schemes in terms of lower incidence of spurious sea ice formation. Here, we use the upwind third-order advection (Leonard et al., 1993; Rasch, 1994; Shchepetkin & McWilliams, 2005), also known as Uniformly Third-Order Polynomial Interpolation Algorithm (UTOPIA), as tracer advection scheme. The K-profile parameterization (KPP) is chosen as a tracer vertical mixing scheme.

The model domain includes 462 (462) x- (y-) grid points with a ∼25-km grid spacing for both ROMS and CICE. The ROMS model uses 40 vertical levels of S-coordinate, and the CICE model uses 7 ice layers, 1 snow layer, and 5 categories of sea ice thickness (default setting). The time step for each model component is set as 600 s, with the coupling frequency between components occurring at each time step. Initial and boundary conditions for the ROMS and CICE models are from the CFSR reanalysis. Atmospheric forcing is provided by the ERA5 6-hourly fields and linearly interpolated to each model timestep.

To validate the experimental feasibility of the model, we evaluated 40-year (1981–2020) control simulation results against observations and reanalysis data. Comparison with observations indicates the model reliably simulates the observed features of SST and SIC, including their spatial distributions and temporal trends (see Figures S1–S3 and Texts S1 and S2 in Supporting Information S1 for more details).

2.3. Experimental Design and Methods

2.3.1. Cyclone Detection and Removal Algorithms

In this study, the latest cyclone detection and tracking algorithm developed by Crawford and Serreze (2016) is used to identify the cyclone tracks and features. This algorithm identifies cyclones using 6-hourly sea level pressure fields, which are projected onto the Southern Hemisphere Equal-Area Scalable Earth 2.0 grid with a resolution of 100 km by 100 km, based on Lambert's equal-area azimuthal projection. It is a Lagrangian method, which is better to provide the information of individual cyclones. As for the criterion of EC, the relative normalized deepening rate ([NDR]r) is typically used to recognize EC (Jena et al., 2022; Lim & Simmonds, 2002; Sanders & Gyakum, 1980; Vichi et al., 2019; Xu et al., 2024). The relative normalized deepening rate ([NDR]r) is calculated using the equation below:

$$[\mathrm{NDR}]_r = \frac{\Delta P_r}{24} \cdot \frac{\sin 60}{\sin|\varnothing|} \tag{1}$$

Where r of [NDR] means the relative central pressure, which is computed as the anomaly with respect to the six-hourly ERA5 SLP climatology at each grid point, which eliminates the differences of background pressure as the cyclone moves toward higher latitudes. **Δ**Pr means the variation of relative central pressure within 24 hr, centered around the time when the cyclone occurs, and ϕ represents the mean latitude during the 24-hr period. When [NDR]r is larger than 1, the cyclone is identified as an EC. The cyclone intensity is quantified by the Laplacian of the mean SLP field (∇^2P) over each grid point where cyclone center is located. Following Lim and Simmonds (2002), when the cyclone with a ∇^2P value greater than 0.7 hPa/10^4 km^2 is classified as a strong one.

Employment of cyclone removal techniques is a powerful way to investigate the effects of a cyclone on the large-scale environment. Many studies have applied this technique to tropical cyclones. The tropical cyclones removal technique proposed by Kurihara et al. (1995) was widely used in the tropical cyclone numerical experiments (Arakane & Hsu, 2020; Cheung & Chan, 1999; Kwon et al., 2002; Rogers et al., 2003). Following this method, we divide atmospheric variable fields into background and disturbance fields. The disturbance domain is determined by cyclone size, which is identified as the area within the last closed isobar with the distance of 2 hPa around the cyclone center.

For dynamic variable fields, such as the pressure field, values within the cyclone domain are replaced with the average of the outermost closed isobar, effectively smoothing the low-pressure center inside the cyclone domain. For zonal or meridional wind fields, the original values within the cyclone domain are replaced with the average of all values in the domain. This approach ensures minimal wind speeds within the cyclone domain after smoothing the low-pressure center, as the absence of a pressure gradient results in negligible wind speeds. The calculation formula is as follows:

$$h_{\mathrm{BR}} = \frac{1}{n}\sum_{i=1}^{n} h_i \tag{2}$$

Here, h_{BR} denotes the replaced variable value within the cyclone domain, while h_i represents the variable values along the outermost closed isobar of the cyclone domain, with a total of n points. For wind fields, h_i corresponds to all values within the cyclone domain.

For thermodynamic variable fields (e.g., temperature, precipitation), the original values inside the cyclone domain undergo a filtering process. Following Kurihara et al. (1993), a zonal three-point spatial smoothing filter is first applied:

$$\overline{h_{\lambda,\varphi}} = h_{\lambda,\varphi} + K(h_{\lambda-1,\varphi} + h_{\lambda+1,\varphi} - 2h_{\lambda,\varphi}) \tag{3}$$

where $\overline{h_{\lambda,\varphi}}$ represents the zonally smoothed value, with subscripts λ and φ denoting longitude and latitude, respectively. Here, $\lambda+1$ and $\lambda-1$ indicate longitudes spaced at 0.25° intervals from λ. The parameter K is the filter coefficient:

$$K = \frac{1}{2}\left(1 - \cos\frac{2\pi}{m}\right)^{-1} \tag{4}$$

The filter in Equation 3 is applied successively for spatial filtering, with the parameter m taking different values in each application: 2, 3, 4, 2, 5, 6, 7, 2, 8, 9, 2. Grid points at the eastern and western boundaries remain unaltered. Following the zonal smoothing, meridional smoothing is similarly performed:

$$h_{B\lambda,\varphi} = \overline{h_{\lambda,\varphi}} + K\left(\overline{h_{\lambda,\varphi-1}} + \overline{h_{\lambda,\varphi+1}} - 2\overline{h_{\lambda,\varphi}}\right) \tag{5}$$

As illustrated in Figure S4 of Supporting Information S1, after the removal of cyclone perturbations, the environmental field retains disturbances outside the cyclone domain. This ensures that only localized cyclone perturbations are removed. Subsequently, both the initial field (h) and the environmental field (h_B) are used as atmospheric forcing fields to drive the model. The differences between their results can then be attributed to the influence of the cyclone perturbation field (h_D).

We conduct two numerical experiments using the ROMS-CICE coupled model. One is the control experiment (CTL) forced with original atmospheric forcing fields, and the other is the sensitivity experiment (hereafter referred to as EXP_noEC) forced with cyclone-removal atmospheric forcing fields. The response of the ocean and sea ice to the cyclone is diagnosed as the difference between CTL and EXP_noEC.

2.3.2. Diagnostics of Physical Processes in the Upper Ocean and Sea Ice

The ROMS model calculates the temperature and salinity tendency equations (see below) in its diagnostic output. The rate of change is determined by four primary factors: horizontal advection (HADV), horizontal diffusion (HDIF), vertical advection (VADV), and vertical diffusion (VDIF). The surface forcing term is not considered as an independent term in the tendency equation, but its effects are included in the advection and diffusion terms (Steffen & Bourassa, 2020).

$$\underbrace{\frac{\partial T}{\partial t}}_{\text{tendency}} = \underbrace{-\left(u\frac{\partial T}{\partial x} + v\frac{\partial T}{\partial y}\right)}_{\text{horizontal advection}} + \underbrace{w\frac{\partial T}{\partial z}}_{\text{vertical advection}} + \underbrace{\frac{\partial}{\partial x}\left(\kappa_h\frac{\partial T}{\partial x}\right) + \frac{\partial}{\partial y}\left(\kappa_h\frac{\partial T}{\partial y}\right)}_{\text{horizontal diffusion}} + \underbrace{\frac{\partial}{\partial z}\left(\kappa_v\frac{\partial T}{\partial z}\right)}_{\text{vertical diffusion}} \tag{6}$$

Here T denotes the tracer (temperature or salinity), and the left term is the tendency in time (°C per day or psu per day). u, v and w are velocities in x-, y-and z-directions, respectively. k_{h} and k_{v} is the horizontal and vertical diffusivity with the value of 150 and 10^{-6} $\mathrm{m^2 s^{-1}}$, separately.

To assess the role of the sea surface slope in the impact of the EC on sea ice, we used the diagnostic term "zeta" from ROMS as the sea surface height (Lee & Kim, 2021; Zhou et al., 2018). It represents the sum of mean

dynamic topography and sea level anomaly—the deviation of the sea surface from the geoid—which is one of several quantities related to sea surface height (Kerry et al., 2016).

To understand the physical factors driving the evolution of Antarctic sea ice, including ice concentration and thickness, we analyze the mass budget of Antarctic sea ice as defined in Notz et al. (2016, Appendix E). This includes sea ice growth in supercooled open water (frazil), sea ice growth at the bottom of the ice (basal growth), sea ice growth due to the transformation of snow into sea ice (snow ice), sea ice melt at the air–ice interface (top melt), sea ice melt at the bottom of the ice (basal melt), sea ice melt at the sides of the ice (lateral melt), and sea ice mass changes due to dynamics-related processes (e.g., advection). These diagnostic variables are determined by recording the ice mass tendency from the above processes separately at every time step and integrating them to output the daily mean values.

3. Results

3.1. Synoptic Features During the EC

We selected an EC that occurred over the southern Pacific Ocean during the 24th −30 April 2002 (among the 34 strong ECs in autumn that passed through the region in Xu et al., 2024). This EC was chosen due to its long duration and the fact that it formed over the ocean and passed through sea ice zone. Figure 1a shows its track with color dots representing the evolution of mean sea level pressure (MSLP) at the cyclone center. The EC generated over the high-latitude open ocean (∼58°S, 166°E) at 06 Universal Time Coordinated (UTC) 24 April 2002 and progressed toward the Antarctic continent following a south-eastward trajectory. In the northern Ross Sea sector (50°S–75°S, 150°E−90°W), a low-pressure anomaly developed over Wilkes Land, Antarctica during the 3 days preceding cyclogenesis (21st–23rd April; Figure S5, Text S4 in Supporting Information S1), accompanied by a blocking high-pressure system to the west. During cyclone formation, a distinct meridional band of high integrated water vapor transport (IVT) emerged near 180°, establishing a pronounced moisture channel between -low and high latitudes (Figure S6, Text S4 in Supporting Information S1). During 24th −26 April 2002, the EC developed and strengthened over the southern Pacific Ocean (55°S–70°S, 170°E −130°W), with the minimum MSLP down to 914.9 hPa at 12 UTC 26th April. Then, it moved into the ice-covered Ross Sea and persisted over sea ice for about 3 days, and finally dissipated near the Ross Ice Shelf at 06 UTC 30th April (Figure 1a).

Figure 1b exhibits features of the EC during its occurrence, including the changes of normalized deepening rate and cyclone intensity (represented as the Laplacian of MSLP). It was considered as EC at 06 UTC 25th April accompanied with [NDR]r of 1.13 at ∼60°S ∼160°W, which means that it deepened by more than 28 hPa in 24-hr interval with a central MSLP of 957.6 hPa (Figure 1b). It became a strong cyclone at 06 UTC 26th April based on the cyclone intensity (reaching the threshold of 0.7). Then, it moved over the sea ice zone where the ice concentration is above 90% and weakened quickly.

The large-scale synoptic conditions of several atmospheric parameters during the EC occurrence are derived from the anomalies with respect to ERA5 daily climatological fields. At 12 UTC 26th April, the central MSLP along the cyclone track reached the minimum, with a negative anomaly of up to 50 hPa over the eastern Ross Sea (Figure 1c). Around the core of the EC, wind speed anomalies can exceed 15 m/s. The strong southward winds on the eastern side and the northward winds on the western side of the cyclone are associated with significant advection of warm and moist air from the Southern Pacific Ocean into the Amundsen Sea, and cold and dry air from the Ross Sea to the north. This leads to a warming anomaly of approximately 5°C over the ice-covered ocean in the eastern region, and a cooling anomaly of about −10°C in the western region (see Figures 1d and 1f). The spatial distribution of downward longwave radiation reveals the vortex structure at the cyclone center, while the increased cloud cover in the peripheral cloud bands leads to an increase (Figure 1e). These characteristics display the mature stage of cloud vortex with spiraling of clear air around the well definite center (Carleton & Carpenter, 1990; Streten & Troup, 1973). Over the eastern area of the cyclone center, there is a positive downward longwave radiation anomaly of about 40–50 W/m^{-2}, which might be associated with the presence of low-level mixed-phase clouds that contributes to the surface air warming. This is consistent with the anomaly of surface temperature in Figure 1f, indicating strong transport of energy between the high and low-latitude during the explosion of the cyclone.

Based on the composite analysis, we can investigate the cyclone structure and roughly estimate the changes of atmospheric environment during the EC development. However, this effect includes the influence of background

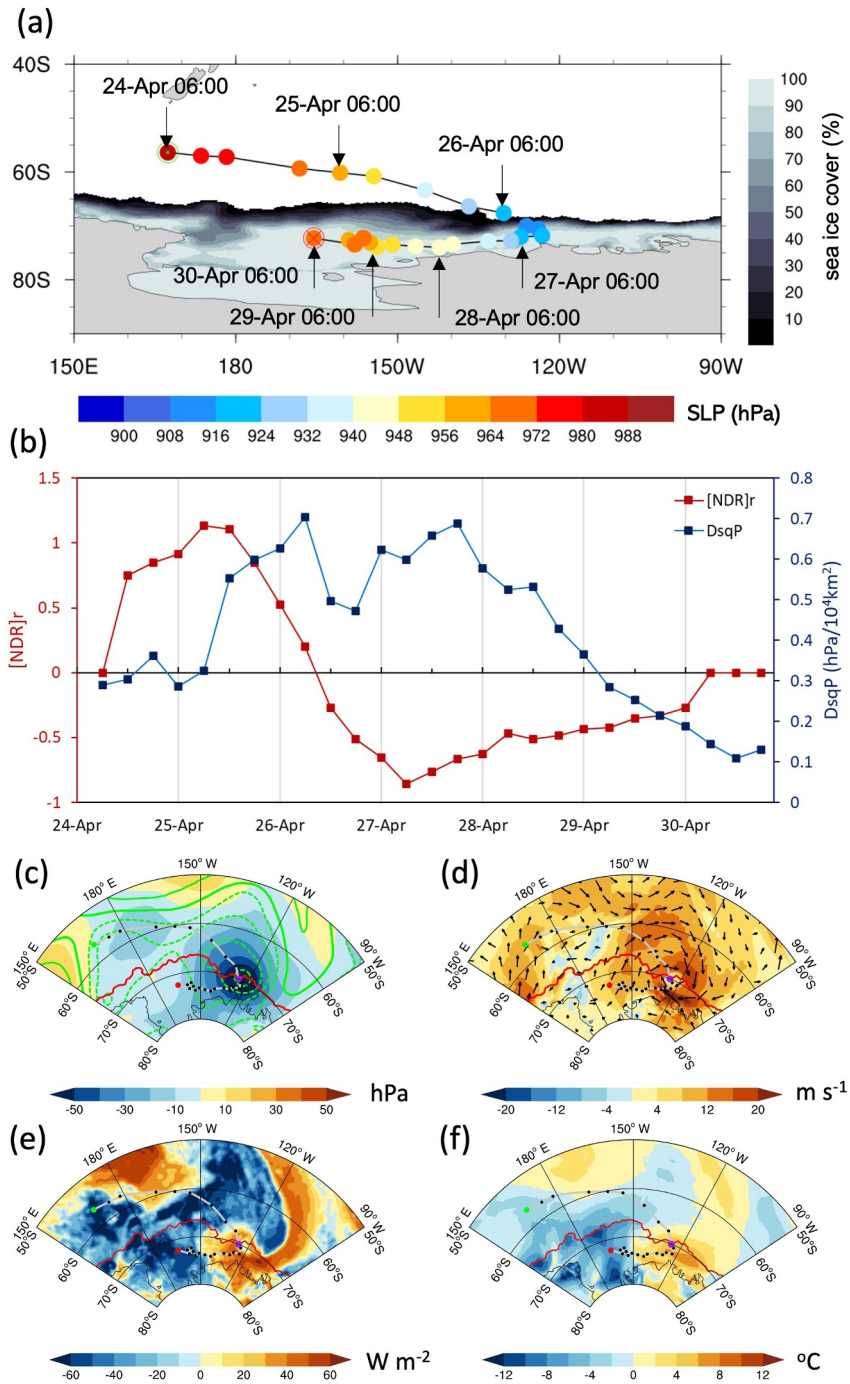

Figure 1. Features of the EC during 24th–30 April 2002: (a) cyclone track with color dots representing the evolution of mean sea level pressure at the cyclone center (The green and red empty circle mark the locations of cyclone generation and dissipation separately), (b) time series of the relative normalized deepening rate (red dot lines) and the Laplacian of mean sea level pressure (blue dot lines). The atmospheric conditions of the EC at 12 UTC 26 April 2002: anomalies with respect to the ERA5 daily climatology of (c) mean sea level pressure (colors) and geopotential height at 500 hPa (contours; the interval is 10 hPa), (d) wind speed at 10 m with direction vectors, (e) downward longwave radiation and (f) surface air temperature at 2 m. The gray line with black dots indicates the cyclone track, and the green, purple and red dots represent the location of cyclone generation, occurrence and dissipation separately. The red line outlines the sea ice edge based on the contour of 15% sea ice concentration from NSIDC.

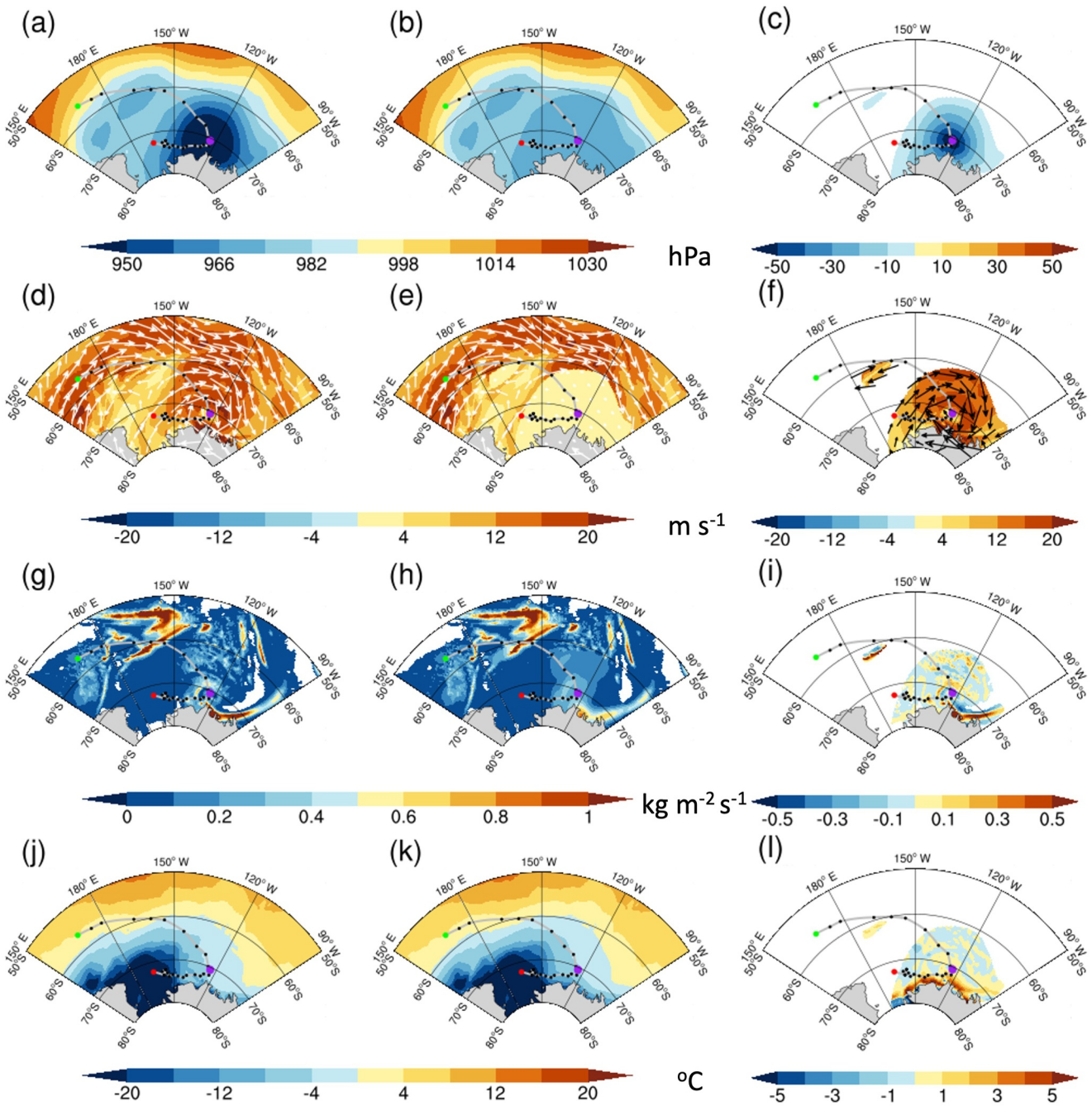

Figure 2. Mean sea level pressure at 12 UTC 26 April 2002 in: (a) original field, (b) cyclone-removed field and (c) the EC component. (d–f), (g–i) (j–l) are the same as the top panel but for 10-m wind, rainfall rate, and 2-m air temperature, separately. The gray line with black dots indicates the cyclone track, and the green, purple and red dots represent the location of cyclone generation, occurrence and dissipation separately.

circulation. To quantify the net effect of the EC, we need to remove its induced dynamic and thermodynamic changes while maintaining the background circulation. Here we use four forcing variables as examples. As shown in the middle column in Figure 2, the features of EC in MSLP, meridional wind, rainfall rate, and air temperature fields are removed within an approximate ellipse domain at around 70°S, 125°W. After removal of the EC, the weak cyclonic circulations remain in the cyclone-removed field which sustain the influences of the background (Figure 2b). The wind speed within the defined cyclone domain is removed but the signs are maintained, ensuring a continuity at the boundaries (Figure 2e). As for thermodynamic fields, the rainfall belt associated with the

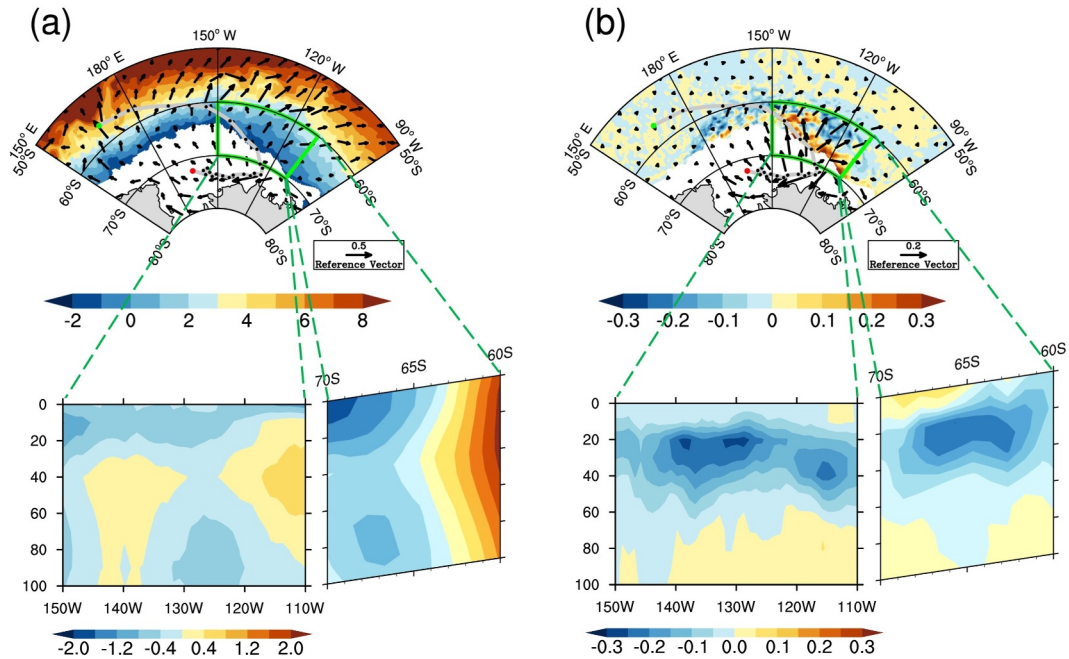

Figure 3. Sea temperature in the upper ocean (100 m) averaged from 27th to 30 April 2002 derived from (a) CTL, (b) the response (CTL minus EXP_noEC). The two vertical cross-section subplots show the zonal average over 60°S–70°S and the meridional average over 110°W–150°W. The gray line with black dots indicates the cyclone track, while the green and red dots represent the location of cyclone generation and dissipation, separately. The arrows indicate the surface ocean currents. The green box highlights the region with maximum response.

circulation of the EC is smoothed and weakened, and the surface air temperature decreases near the coast (Figures 2h and 2k). Outside the defined cyclone domain, the characteristics of circulation remain unchanged to avoid the influences of other regions. The differences between original and cyclone-removed fields in the right column in Figure 2 represent the net EC components, indicating that the central MSLP of above 40 hPa and meridional wind of up to 12 m/s have been removed, along with the smoothed rainfall belt and surface air temperature. Next, these original fields and cyclone-removed fields are separately applied to the ocean-ice coupled model as the atmospheric forcing to investigate the impacts of the EC on the upper ocean and sea ice.

3.2. Impacts of the EC on the Upper Ocean

The control state (CTL; with EC) and response (CTL minus EXP_noEC) of sea temperature in the upper ocean to the EC are shown in Figure 3. During the period of 3 days after EC generation to the day of cyclolysis, the strong clockwise wind stress associated with the EC imparts positive vorticity into the ocean, inducing surface cyclonic divergence around the cyclone center. This intensifies northward ocean currents and triggers the upwelling of subsurface water. Accompanied by the ocean current response, the sea surface temperature response occurs along the EC trajectory. This response developed and strengthened near the ice edge when the EC crossed over sea ice (Figure S8 in Supporting Information S1). As shown in Figure 3b, sea surface warming of up to 0.20°C occurs along the sea ice edge, while a cooling of about −0.15°C is observed at the outer circle of the EC trajectory. The response of sea temperature in the upper ocean, averaged within the green box in Figure 3b (60°S–70°S, 110°W–150°W), indicates that the impact on sea temperature is not confined to the sea surface. This warming response could extend down to about 20 m, accompanied by a strong cooling response in the upper ocean from a depth of 20–60 m.

Meanwhile, an increase in sea surface salinity exceeding 0.20 practical salinity units (psu) is observed within the region outlined by the green box, and the response extends to a depth of around 25 m (Figure 4b; refer Figure S9 in Supporting Information S1 for each day during cyclone period). This increase is followed by a decrease in salinity at depths of 30–60 m. The pattern is analogous to the temperature response and is likely driven by intensified

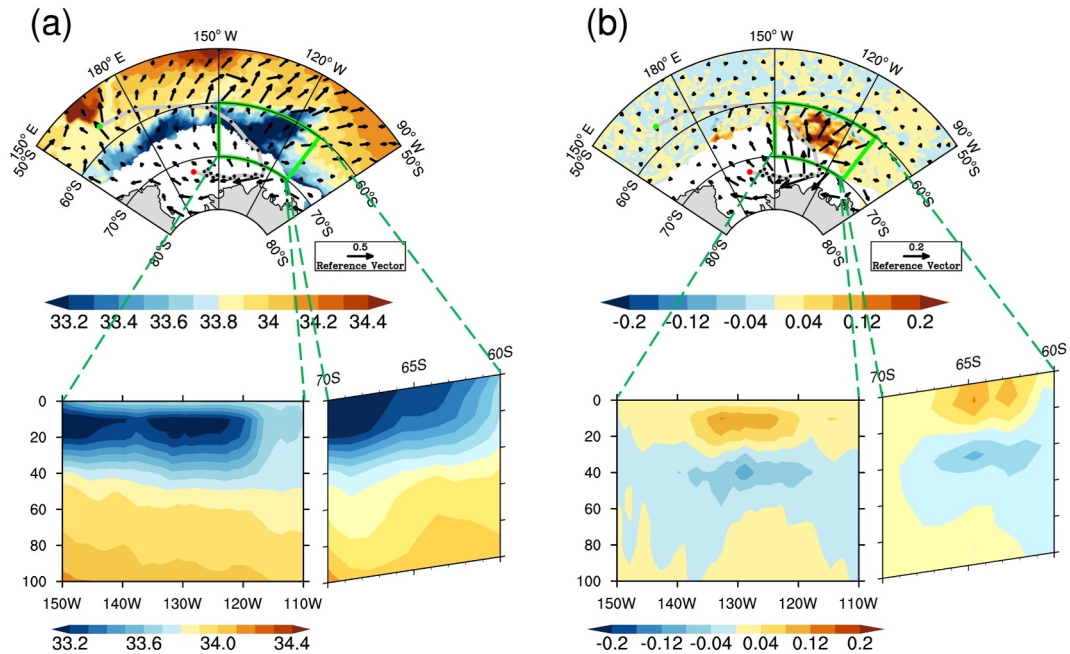

Figure 4. Same as Figure 3 but for sea salinity (practical salinity units; psu).

vertical mixing due to surface divergence. This enhanced mixing deepens the boundary layer and promotes greater diffusion between the more saline water below 20 m and the fresher water above (Figure 4a). The contrasting responses between the surface and subsurface ocean layers highlight the stirring effect induced by the EC, which introduces significant perturbations to the sea surface and deepens the upper ocean boundary layer.

To better quantify the upwelling intensification mentioned above, we conducted a volume flux budget analysis over the green box region following the methodology of Liao et al. (2024; see Text S5 in Supporting Information S1 for details). In the upper-layer volume flux budget, vertical transport at 30 m depth, Ekman transport, and coastal Ekman transport are all significant contributors to upwelling (Figures S7a and S7b in Supporting Information S1). As shown in Figure S7c of Supporting Information S1, it is clear that the total vertical transport and Ekman pumping dominates the upwelling change during the cyclone period. The coastal Ekman transport exhibits a negative contribution to upwelling, while the total geostrophic outflow remains weakest and nearly negligible.

Here, we consider the surface ocean layer (0–20 m) and the subsurface ocean layer (20–60 m) separately to determine the dominant processes responsible for the observed temperature and salinity responses. We investigate the contribution of each individual process in the temperature tendency equation, including temperature advection (combined effect of horizontal and vertical advection), horizontal diffusion, and vertical diffusion for both the surface and subsurface ocean layers (see Figures 5a–5d and 5e–5h). In the region exhibiting sea surface temperature (SST) warming responses around the cyclone core (Figure 3b), there is a warming tendency exceeding 0.2°C per day near the sea ice edge and along the coast (Figure 5a). This warming is predominantly driven by vertical diffusion (Figure 5d) and is attributed to the upwelling of subsurface warm water, which mixes with the colder surface water due to anomalous surface cyclonic divergence. In contrast, the area outside the cyclone core displays a cooling response in SST (Figure 3b), characterized by a surface cooling tendency (Figure 5a). This cooling is primarily driven by temperature advection associated with the northern branch of cyclonic winds, which transport cold surface water from regions near the sea ice into this area (Figure 5b). The spatial distributions of the horizontal and vertical advection components are relatively chaotic and partially offset each other (see Figure S10 in Supporting Information S1); hence, we combine them into a single advection term (Figures 5b and 5f). In the subsurface ocean layer, the cooling tendency (Figure 5e) is predominantly linked to vertical temperature diffusion (Figure 5h).

The contributions of various ocean processes to the increase in salinity, as described in the salinity tendency equation, were examined. These processes include salinity advection, horizontal diffusion, and vertical diffusion

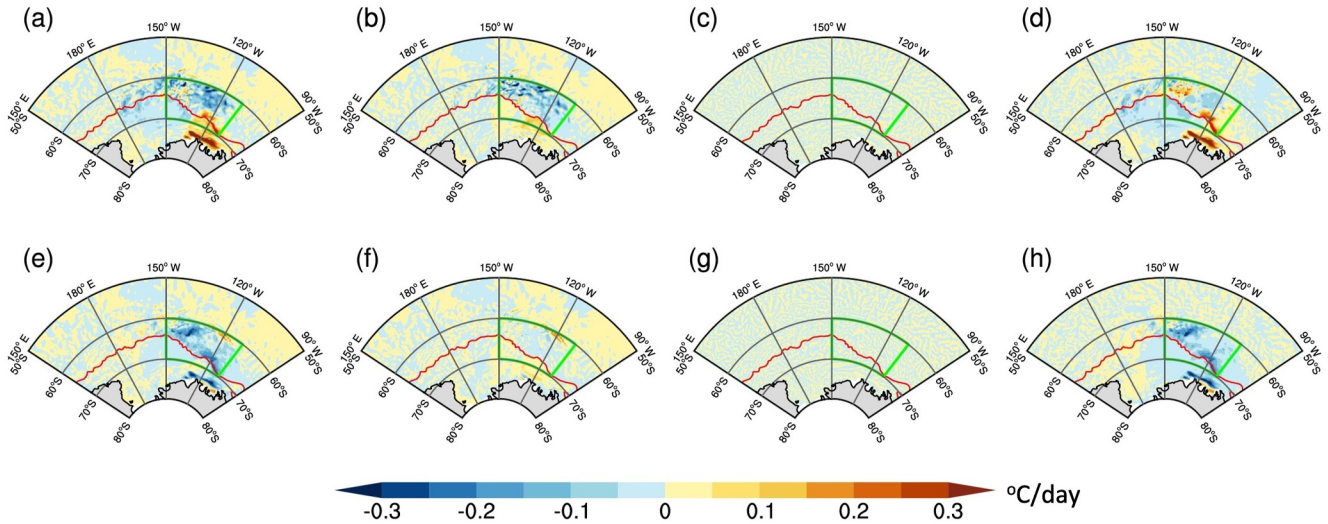

Figure 5. The response (CTL minus EXP_noEC) of the terms in the temperature tendency equation for the upper ocean layer averaged within the depth of 0–20 m: (a) temperature tendency, (b) temperature advection, (c) horizontal diffusion and (d) vertical diffusion on 26 April 2002. (e–h) are the same as (a–d) but for the upper ocean layer averaged within the depth of 20–60 m. The red line indicates the sea ice edge based on the contour of 15% sea ice concentration. The green box highlights the region with maximum response.

(refer to Figure S11 in Supporting Information S1 for details on individual advection terms). In the region exhibiting an increasing salinity response around the cyclone core (Figure 4b), there is an increase of approximately 0.16 psu per day in the surface ocean layer, accompanied by a relatively weaker decrease in the areas surrounding the cyclone core (Figure 6a). As illustrated in Figures 6b and 6d, vertical diffusion plays a crucial role in generating the salinity response near the cyclone core, while advection is primarily responsible for the salinity changes observed in the periphery of the cyclone. Meanwhile, a weak decreasing tendency in salinity is noted in the subsurface layer, which is mainly attributed to the effects of vertical diffusion.

The EC was generated on 24th April, met the criteria for EC formation on 25th April, and finally dissipated on 30th April (Figure 1b). Although it persisted for 6–7 days, its effects on the upper ocean can sustain for a longer period. Figure 7 shows the evolution of sea temperature and salinity, area-averaged in the green box shown in

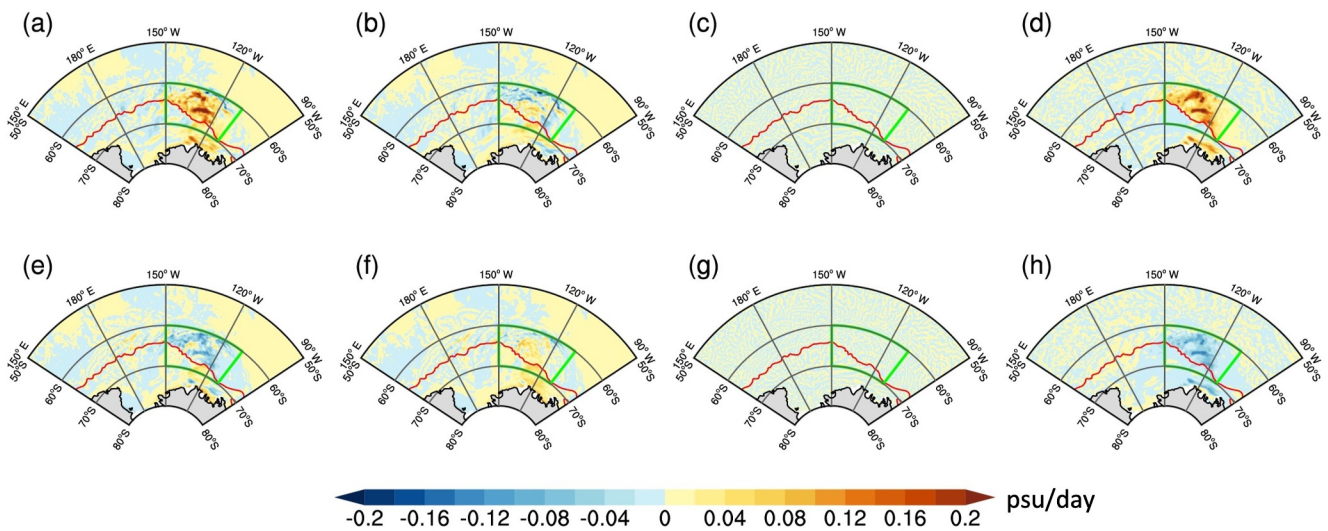

Figure 6. The response (CTL minus EXP_noEC) of the terms in the salinity tendency equation for the upper ocean layer averaged within the depth of 0–20 m: (a) salinity tendency, (b) salinity advection, (c) horizontal diffusion and (d) vertical diffusion on 26 April 2002. (e–h) are the same as (a–d) but for the upper ocean layer averaged within the depth of 20–60 m. The red line indicates the sea ice edge based on the contour of 15% sea ice concentration. The green box highlights the region with maximum response.

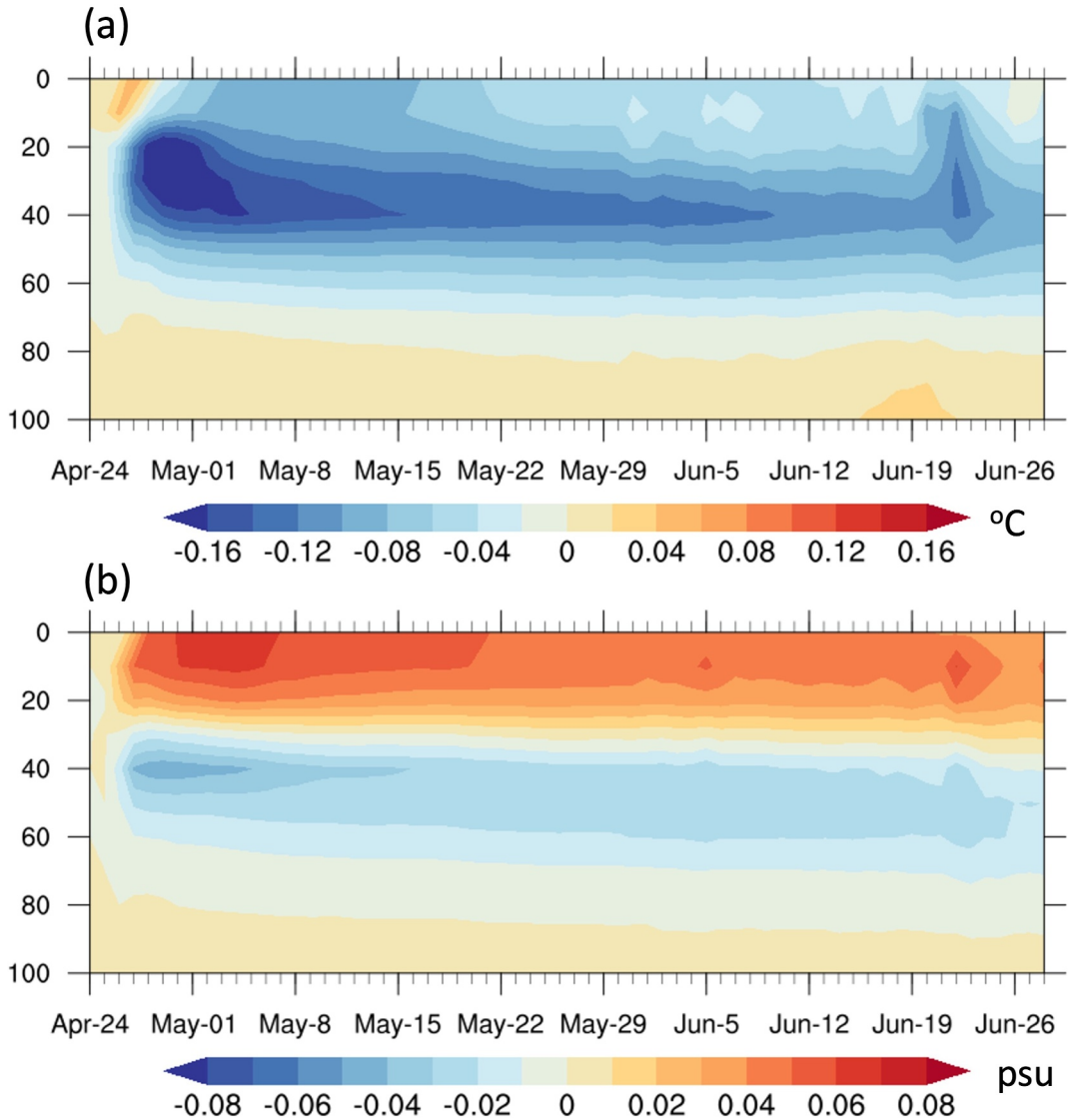

Figure 7. The area-averaged response (CTL minus EXP_noEC) in the upper ocean during the cyclone period and the following month for the responses of (a) sea temperature and (b) sea salinity. The averages are taken over the key region (110°W–150°W, 60°S–70°S), as outlined by the green box in Figure 3a.

Figure 3b, during the occurrence period and the following month. The area-averaged surface warming response is enhanced for approximately 3–4 days after the EC event (on 25th April), reaching around 0.06°C, and then dissipates quickly. In contrast, the subsurface cooling response intensified for about 4–5 days after the EC generation, reaching up to −0.16°C at around 40 m depth. This subsurface cooling response gradually weakens thereafter, stabilizing at a relatively minor cold anomaly approximately 4 weeks later (on 22nd May). The cooling response exceeding 0.08°C is primarily observed between 30 and 50 m depth, but its effect can extend down to 100 m. It is intuitive that the sea surface temperature anomaly recovers quicker than subsurface due to the exchange of heat flux with atmosphere at the air-sea interface. The increasing sea salinity response occurs in the upper ocean layer down to 30 m, peaking at the surface with a change of more than 0.06 psu. This response gradually diminished, stabilizing after approximately 6 weeks (around 7th June) with a residual anomaly of 0.03–0.04 psu. The decreasing response in the subsurface ocean layer reduces slightly quicker than surface, eventually stabilizing at a negative anomaly of less than 0.02 psu between 40 and 70 m depth.

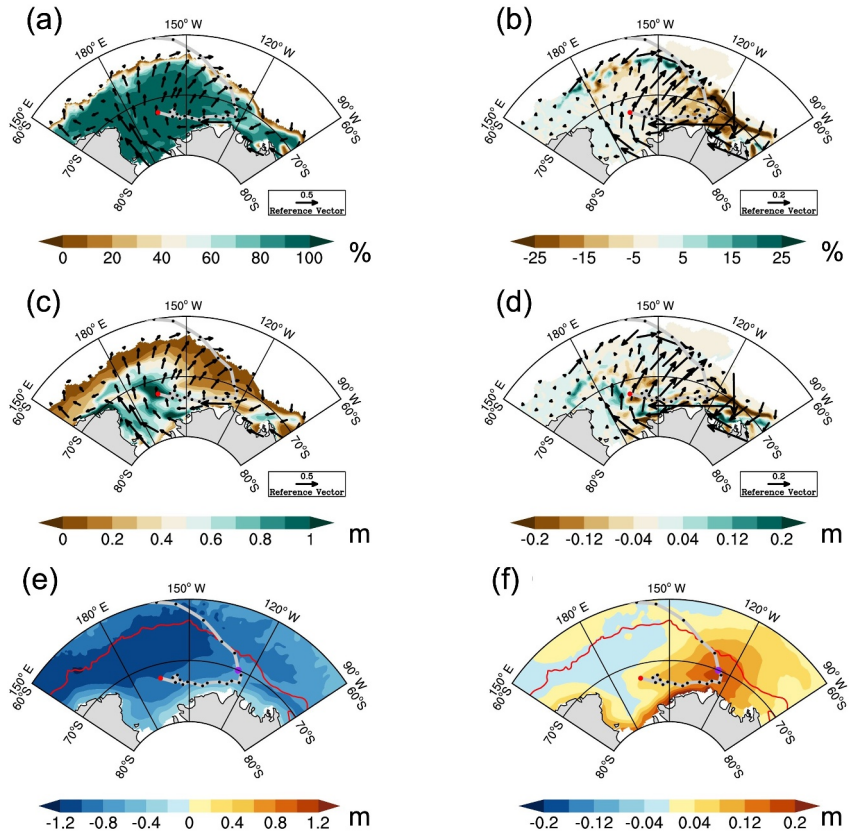

Figure 8. Sea ice response averaged during 27th–30 April 2002: sea ice concentration derived from (a) CTL, (b) the response (CTL minus EXP_noEC). (c, d), (e, f) are the same as (a, b) but for sea ice thickness and sea surface height. The gray line with black dots indicates the cyclone track. The black arrows indicate the ice drifts, while the red line outlines the sea ice edge based on the contour of 15% sea ice concentration.

3.3. The Impacts of the EC on Sea Ice

In addition to the impacts of the EC on the upper ocean, it can also influence sea ice when it passes through the edge of sea ice. In the CTL state, sea ice concentration is less than 60% and sea ice thickness is less than 0.4 m along the edge, due to the forcing of wind stress and ocean currents (Figures 8a and 8c).

During the cyclone period, the EC crossing the ice edge results in onshore winds on the eastern side of the EC that break up the ice and push it inland (Figures 8b and 8d). The wind-induced sea surface ocean slope could cause the iceberg calving (Francis et al., 2021). It can be observed that the cyclonic wind induced a strong slope on the sea surface, accompanied by height anomalies exceeding 0.1 m (Figure 8f). This process leads to a significant reduction in sea ice concentration and thickness along the edge, with anomalies reaching as low as −25% in concentration and −0.2 m in thickness (refer Figures S12 and S13 in Supporting Information S1 for each day). At the western side of the EC, the offshore wind induces a light increase of sea ice thickness within the edge.

Here we assessed the EC's impact on sea ice by analyzing sea ice mass fluxes, including snow ice formation, frazil ice growth, congelation ice growth, lateral ice melt, basal ice melt, top ice melt, and dynamic ice changes (Figure 9). The spatial distribution and magnitude of sea ice changes induced by dynamic processes, illustrated in Figure 9g, are broadly consistent with the total sea ice changes depicted in Figure 9h, with the most significant decrease exceeding 3 cm/day around Antarctica. Basal ice melting emerges as the primary contributor to the reduction in sea ice (Figure 9e), linked to the warm ocean currents transported to the coast. In contrast, the other mass fluxes exhibit non-uniform distributions and considerably smaller values, suggesting their limited contribution to the instantaneous sea ice changes induced by the EC.

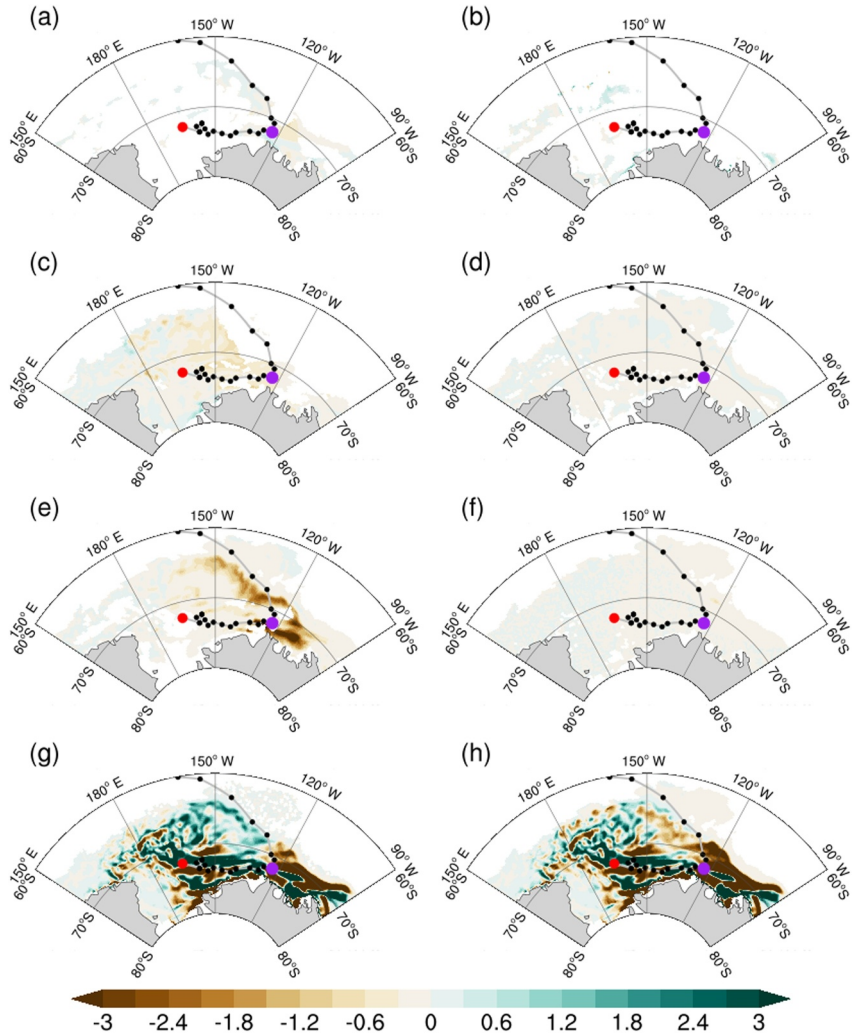

Figure 9. The response (CTL minus EXP_noEC) of each contributor in the sea ice mass fluxes (cm/day) for sea ice concentration formation: (a) snow ice formation, (b) frazil ice growth, (c) congelation ice growth, (d) lateral ice melt, (e) basal ice melt, (f) top ice melt, (g) dynamic ice change, and (h) total ice response on 26 April 2002.

4. Discussions and Conclusions

In this study, we investigate the impacts of an EC over the Southern Pacific Ocean on the upper ocean and sea ice by employing a cyclone-removal method in our modeling experiments. The results show notable responses in the upper ocean the day after the EC's explosion: the strong clockwise wind stress generates surface cyclonic divergence, which enhances northward ocean currents and induces upwelling of subsurface water. A sea surface warming response of up to 0.20°C is observed near the EC center, accompanied by a cooling response of up to −0.15°C at the EC periphery. Beneath this surface temperature anomaly, significant cooling of exceeding 0.15°C occurs in the subsurface ocean layer at depths of 20–60 m. Concurrently, sea surface salinity exhibits increasing response of up to 0.20 psu, accompanied by decreasing response in the subsurface layer at depths of 30–60 m. When the EC traversed the ice-covered Ross Sea, it resulted in a reduction in sea ice concentration and thickness along the ice edge, with anomalies of approximately −25% and −0.2 m, respectively. The changes induced by the EC are relatively smaller than those reported in previous studies (Jena et al., 2022; Vichi et al., 2019). This might be due to the influence of the background circulation not being removed in their studies.

Many atmospheric and oceanic factors contribute to the abrupt changes observed in the upper ocean induced by EC. Some studies have noted the challenges of quantifying the relative roles of individual factors due to limited data availability (Turner et al., 2020; Vichi et al., 2019). However, the relative contributions of each process can

be assessed within the modeling simulation. During the EC event, the responses of surface temperature and salinity are primarily attributed to vertical diffusion near the cyclone core and advection in the periphery of the cyclone. Regarding subsurface ocean layers, vertical diffusion is the predominant factor responsible for the cooling and decreasing salinity. In terms of sea ice change, mass balance budget analyses indicate that dynamic processes play the leading role in altering ice conditions, followed by basal ice melting.

Although some studies have suggested that the effects of EC on ocean conditions and sea ice may extend beyond the dissipation of EC (Jena et al., 2022; Turner et al., 2020; Vichi et al., 2019), very limited research has accurately quantified the persistence of these impacts on ocean parameters induced by ECs. Research on tropical cyclones indicates that their effects on sea surface temperature can recover within several days to weeks (Emanuel, 2001; Hart et al., 2007; Wang et al., 2016), while changes in sea salinity in the upper ocean can persist for approximately 10–12 days (Girishkumar et al., 2014). Here, our model sensitivity simulations demonstrate that the impacts of ECs on ocean temperature and salinity can last for over 4 weeks, with residual anomalies detectable for more than 1 month. Notably, the larger anomalies observed in the subsurface ocean layer, particularly at depths of 20–60 m, may persist for an even longer duration. Additionally, a series of extratropical cyclones frequently occur over the Southern Ocean, influencing the upper ocean and sea ice in a sustained manner; however, their cumulative effects remain an open question. Further research is warranted to address this issue.

The cyclone removal method adopted in this study could isolate the effects of cyclones, but several limitations remain. First, the identification of cyclonic regions was based on isobaric contours, which may result in insufficient removal of wind anomalies in the outer portions of cyclones. For thermodynamic fields, the cyclone-associated components typically exhibit asymmetric spatial structures, which can only be mitigated through filtering techniques—often with limited effectiveness. Consequently, the results may underestimate the role of cyclonic components. Second, the findings are derived solely from the ROMS-CICE coupled model, and uncertainties inherent in model simulations may affect the magnitude of the responses. Future work should consider ensemble simulations with multiple models or validate the results against observational data to assess their robustness and accuracy. Finally, regarding the duration of subsurface temperature and salinity anomalies induced by the EC, it should be emphasized that model results may deviate from real-world conditions. Because the ROMS-CICE model used here is not coupled with an atmospheric component, the oceanic changes induced by cyclonic forcing cannot feed back to the atmosphere. In the real ocean–atmosphere system, such adjustment and air–sea interactions would likely shorten the persistence of the anomalies. However, in this experiment, the atmosphere is prescribed as an external forcing, and without atmospheric feedbacks, the cyclone-induced oceanic responses tend to persist longer than they would in nature.

We also examined the results of model experiments conducted without removing the thermodynamic fields, finding that they were consistent with the current results presented here (not shown). This finding aligns with the established understanding that the dynamic forcing exerted by cyclones on the ocean is more pronounced. Nonetheless, it is important to note that the air-sea interaction processes are inherently complex. For instance, the sea spray process plays a significant role in mediating the transport of heat and momentum fluxes at the air-sea interface. According to previous research, sea spray is responsible for over 10% of the total air-sea heat and momentum fluxes, particularly under conditions of strong wind speeds (Andreas et al., 2008, 2015). Given its notable thermal and dynamical effects, the influence of sea spray should be considered during events associated with strong wind stress. Future research should employ coupled models that incorporate sea spray parameterization to simulate and quantify the impacts highlighted in the cyclone-removal experiments discussed above more accurately.

Data Availability Statement

The ERA5 hourly data on single level is provided by Copernicus Climate Change Service (C3S) Climate Data Store (CDS) DOI: 10.24381/cds.adbb2d47 (Accessed on 01-02-2021) at https://cds.climate.copernicus.eu/datasets/reanalysis-era5-single-levels?tab=download. The National Snow and Ice Data Center (NSIDC) Climate Data Record of Passive Microwave Sea Ice Concentration (Version 4) is obtained at https://nsidc.org/data/g02202/versions/4. The ocean and sea ice data used to establish the boundary conditions were obtained from the National Centers for Environmental Prediction (NCEP) Climate Forecast System Reanalysis (CFSR), DOI: 10.5065/D69K487J, which is available at https://doi.org/10.5065/D69K487J (Accessed on 15-10-2022).

Acknowledgments
This research is supported by the National Key R&D Program of China (2024YFF0506600), National Natural Science Foundation of China (42376237), and the Southern Marine Science and Engineering Guangdong Laboratory (Zhuhai) (SML2024SP023) and the National Key Scientific and Technological Infrastructure project "Earth System Science Numerical Simulator Facility" (Earth Lab).

References

Andreas, E. L., Mahrt, L., & Vickers, D. (2015). An improved bulk air–sea surface flux algorithm, including spray-mediated transfer. *Quarterly Journal of the Royal Meteorological Society*, *141*(687), 642–654. https://doi.org/10.1002/qj.2424

Andreas, E. L., Persson, P. O. G., & Hare, J. E. (2008). A bulk Turbulent air–sea flux algorithm for high-wind, spray conditions. *Journal of Physical Oceanography*, *38*(7), 1581–1596. https://doi.org/10.1175/2007JPO3813.1

Arakane, S., & Hsu, H.-H. (2020). A tropical cyclone removal technique based on potential vorticity inversion to better quantify tropical cyclone contribution to the background circulation. *Climate Dynamics*, *54*(5–6), 3201–3226. https://doi.org/10.1007/s00382-020-05165-x

Ashley, W. S., & Black, A. W. (2008). Fatalities associated with Nonconvective high-wind events in the United States. *Journal of Applied Meteorology and Climatology*, *47*(2), 717–725. https://doi.org/10.1175/2007JAMC1689.1

Bengtsson, L., Hodges, K. I., & Keenlyside, N. (2009). Will extratropical storms intensify in a warmer climate? *Journal of Climate*, *22*(9), 2276–2301. https://doi.org/10.1175/2008JCLI2678.1

Bi, D., Dix, M., Marsland, S., O'Farrell, S., Sullivan, A., Bodman, R., et al. (2020). Configuration and spin-up of ACCESS-CM2, the new generation Australian community climate and Earth system simulator coupled model. *Journal of Southern Hemisphere Earth Systems Science*, *70*(1), 225–251. https://doi.org/10.1071/ES19040

Bitz, C. M., Holland, M. M., Weaver, A. J., & Eby, M. (2001). Simulating the ice-thickness distribution in a coupled climate model. *Journal of Geophysical Research*, *106*(C2), 2441–2463. https://doi.org/10.1029/1999JC000113

Bracegirdle, T. J., & Kolstad, E. W. (2010). Climatology and variability of Southern Hemisphere marine cold-air outbreaks. *Tellus A: Dynamic Meteorology and Oceanography*, *62*(2), 202. https://doi.org/10.1111/j.1600-0870.2009.00431.x

Bruneau, N., & Toumi, R. (2016). A fully-coupled atmosphere-ocean-wave model of the Caspian Sea. *Ocean Modelling*, *107*, 97–111. https://doi.org/10.1016/j.ocemod.2016.10.006

Carleton, A. M., & Carpenter, D. A. (1990). Satellite climatology of "polar lows" and broadscale climatic associations for the Southern Hemisphere. *International Journal of Climatology*, *10*(3), 219–246. https://doi.org/10.1002/joc.3370100302

Catto, J. L., Madonna, E., Joos, H., Rudeva, I., & Simmonds, I. (2015). Global relationship between fronts and warm conveyor belts and the impact on extreme precipitation. *Journal of Climate*, *28*(21), 8411–8429. https://doi.org/10.1175/JCLI-D-15-0171.1

Chang, E. K. M. (2017). Projected significant increase in the number of extreme extratropical cyclones in the southern Hemisphere. *Journal of Climate*, *30*(13), 4915–4935. https://doi.org/10.1175/JCLI-D-16-0553.1

Chang, E. K. M., Guo, Y., & Xia, X. (2012). CMIP5 multimodel ensemble projection of storm track change under global warming. *Journal of Geophysical Research*, *117*(D23), 2012JD018578. https://doi.org/10.1029/2012JD018578

Cheung, K. K. W., & Chan, J. C. L. (1999). Ensemble forecasting of tropical cyclone motion using a barotropic model. Part I: Perturbations of the environment. *Monthly Weather Review*, *127*(6), 1229–1243. https://doi.org/10.1175/1520-0493(1999)127<1229:EFOTCM>2.0.CO;2

Colle, B. A., Buonaiuto, F., Bowman, M. J., Wilson, R. E., Flood, R., Hunter, R., et al. (2008). New York city's vulnerability to coastal flooding: Storm surge modeling of past cyclones. *Bulletin of the American Meteorological Society*, *89*(6), 829–842. https://doi.org/10.1175/2007BAMS2401.1

Crawford, A. D., & Serreze, M. C. (2016). Does the summer Arctic frontal zone influence Arctic ocean cyclone activity? *Journal of Climate*, *29*(13), 4977–4993. https://doi.org/10.1175/JCLI-D-15-0755.1

Emanuel, K. (2001). Contribution of tropical cyclones to meridional heat transport by the oceans. *Journal of Geophysical Research*, *106*(D14), 14771–14781. https://doi.org/10.1029/2000JD900641

Francis, D., Eayrs, C., Cuesta, J., & Holland, D. (2019). Polar cyclones at the origin of the reoccurrence of the Maud rise polynya in Austral winter 2017. *Journal of Geophysical Research: Atmospheres*, *124*(10), 5251–5267. https://doi.org/10.1029/2019JD030618

Francis, D., Fonseca, R., Mattingly, K. S., Marsh, O. J., Lhermitte, S., & Cherif, C. (2022). Atmospheric triggers of the brunt ice shelf calving in February 2021. *Journal of Geophysical Research: Atmospheres*, *127*(11), e2021JD036424. https://doi.org/10.1029/2021JD036424

Francis, D., Mattingly, K. S., Lhermitte, S., Temimi, M., & Heil, P. (2021). Atmospheric extremes caused high ocean ward sea surface slope triggering the biggest calving event in more than 50 years at the Amery Ice Shelf. *The Cryosphere*, *15*(5), 2147–2165. https://doi.org/10.5194/tc-15-2147-2021

Francis, D., Mattingly, K. S., Temimi, M., Massom, R., & Heil, P. (2020). On the crucial role of atmospheric rivers in the two major Weddell Polynya events in 1973 and 2017 in Antarctica. *Science Advances*, *6*(46), eabc2695. https://doi.org/10.1126/sciadv.abc2695

Girishkumar, M. S., Suprit, K., Chiranjivi, J., Udaya Bhaskar, T. V. S., Ravichandran, M., Shesu, R. V., & Pattabhi Rama Rao, E. (2014). Observed oceanic response to tropical cyclone Jal from a moored buoy in the south-western Bay of Bengal. *Ocean Dynamics*, *64*(3), 325–335. https://doi.org/10.1007/s10236-014-0689-6

Grieger, J., Leckebusch, G. C., Raible, C. C., Rudeva, I., & Simmonds, I. (2018). Subantarctic cyclones identified by 14 tracking methods, and their role for moisture transports into the continent. *Tellus A: Dynamic Meteorology and Oceanography*, *70*(1), 1454808. https://doi.org/10.1080/16000870.2018.1454808

Haidvogel, D. B., Arango, H., Budgell, W. P., Cornuelle, B. D., Curchitser, E., Di Lorenzo, E., et al. (2008). Ocean forecasting in terrain-following coordinates: Formulation and skill assessment of the regional Ocean modeling system. *Journal of Computational Physics*, *227*(7), 3595–3624. https://doi.org/10.1016/j.jcp.2007.06.016

Haidvogel, D. B., Wilkin, J. L., & Young, R. (1991). A semi-spectral primitive equation ocean circulation model using vertical sigma and orthogonal curvilinear horizontal coordinates. *Journal of Computational Physics*, *94*(1), 151–185. https://doi.org/10.1016/0021-9991(91)90141-7

Hart, R. E., Maue, R. N., & Watson, M. C. (2007). Estimating local memory of tropical cyclones through MPI anomaly evolution. *Monthly Weather Review*, *135*(12), 3990–4005. https://doi.org/10.1175/2007MWR2038.1

Hersbach, H., Bell, B., Berrisford, P., Hirahara, S., Horányi, A., Muñoz-Sabater, J., et al. (2020). The ERA5 global reanalysis. *Quarterly Journal of the Royal Meteorological Society*, *146*(730), 1999–2049. https://doi.org/10.1002/qj.3803

Hersbach, H., de Rosnay, P., Bell, B., Schepers, D., Simmons, A. J., Soci, C., et al. (2018). Operational global reanalysis: Progress, future directions and synergies with NWP. *ERA Report Series No. 27, ECMWF*. 10.21957/tkic6g3wm

Hoskins, B. J., & Hodges, K. I. (2005). A new perspective on southern Hemisphere storm tracks. *Journal of Climate*, *18*(20), 4108–4129. https://doi.org/10.1175/JCLI3570.1

Hunke, E., Allard, R., Bailey, D. A., Blain, P., Craig, A., Damsgaard, A., et al. (2018). CICE-Consortium/CICE: CICE version 6.0.0 (version CICE6.0.0). *Zenodo*. https://doi.org/10.5281/ZENODO.1900639

Hunke, E. C., Lipscomb, W. H., Turner, A. K., Jeffery, N., & Elliott, S. (2015). *Cice: The Los Alamos Sea ice model documentation and software user's manual version 5.1 LA-CC-06-012. T-3 Fluid Dynamics Group* (Vol. 675, p. 15). Los Alamos National Laboratory.

Jena, B., Bajish, C. C., Turner, J., Ravichandran, M., Anilkumar, N., & Kshitija, S. (2022). Record low sea ice extent in the Weddell Sea, Antarctica in April/May 2019 driven by intense and explosive polar cyclones. *Npj Climate and Atmospheric Science*, *5*(1), 19. https://doi.org/10.1038/s41612-022-00243-9

Kerry, C., Powell, B., Roughan, M., & Oke, P. (2016). Development and evaluation of a high-resolution reanalysis of the East Australian current region using the Regional Ocean Modelling System (ROMS 3.4) and Incremental Strong-constraint 4-Dimensional Variational (IS4D-Var) data assimilation. *Geoscientific Model Development*, *9*(10), 3779–3801. https://doi.org/10.5194/gmd-9-3779-2016

Kumar, R., Li, J., Hedstrom, K., Babanin, A. V., Holland, D. M., Heil, P., & Tang, Y. (2021). Intercomparison of Arctic sea ice simulation in ROMS-CICE and ROMS-Budgell. *Polar Science*, *29*, 100716. https://doi.org/10.1016/j.polar.2021.100716

Kurihara, Y., Bender, M. A., & Ross, R. J. (1993). An initialization scheme of hurricane models by vortex specification. *Monthly Weather Review*, *121*(7), 2030–2045. https://doi.org/10.1175/1520-0493(1993)121<2030:AISOHM>2.0.CO;2

Kurihara, Y., Bender, M. A., Tuleya, R. E., & Ross, R. J. (1995). Improvements in the GFDL hurricane prediction system. *Monthly Weather Review*, *123*(9), 2791–2801. https://doi.org/10.1175/1520-0493(1995)123<2791:IITGHP>2.0.CO;2

Kwon, H. J., Won, S.-H., Ahn, M.-H., Suh, A.-S., & Chung, H.-S. (2002). GFDL-type typhoon initialization in MM5. *Monthly Weather Review*, *130*(12), 2966–2974. https://doi.org/10.1175/1520-0493(2002)130<2966:GTTIIM>2.0.CO;2

Lee, E. A., & Kim, S. Y. (2021). A diagnosis of surface currents and sea surface heights in a coastal region. *Continental Shelf Research*, *226*, 104486. https://doi.org/10.1016/j.csr.2021.104486

Leonard, B., MacVean, M., & Lock, A. (1993). *Positivity-preserving numerical schemes for multidimensional advection* (Vol. 93, p. 27091). NASA STI/Recon Technical Report N.

Liao, F., Yang, K., Wang, Y., Hoteit, I., & Zhan, P. (2024). Future change in the Vietnam upwelling under a high-emission scenario. *Geophysical Research Letters*, *51*(11), e2024GL108305. https://doi.org/10.1029/2024GL108305

Lim, E.-P., & Simmonds, I. (2002). Explosive cyclone development in the southern Hemisphere and a comparison with northern Hemisphere events. *Monthly Weather Review*, *130*(9), 2188–2209. https://doi.org/10.1175/1520-0493(2002)130<2188:ECDITS>2.0.CO;2

Lin, P., Zhong, R., Yang, Q., Clem, K. R., & Chen, D. (2023). A record-breaking cyclone over the Southern Ocean in 2022. *Geophysical Research Letters*, *50*(14), e2023GL104012. https://doi.org/10.1029/2023GL104012

Lipscomb, W. H. (2001). Remapping the thickness distribution in sea ice models. *Journal of Geophysical Research*, *106*(C7), 13989–14000. https://doi.org/10.1029/2000JC000518

Maksym, T. (2019). Arctic and Antarctic Sea Ice change: Contrasts, commonalities, and causes. *Annual Review of Marine Science*, *11*(1), 187–213. https://doi.org/10.1146/annurev-marine-010816-060610

Meier, W., Fetterer, F., Windnagel, A., & Stewart, S. (2021). NOAA/NSIDC climate data Record of passive Microwave Sea Ice concentration, version 4 [Dataset]. *NSIDC*. https://doi.org/10.7265/EFMZ-2T65

Naughten, K. A., Galton-Fenzi, B. K., Meissner, K. J., England, M. H., Brassington, G. B., Colberg, F., et al. (2017). Spurious sea ice formation caused by oscillatory ocean tracer advection schemes. *Ocean Modelling*, *116*, 108–117. https://doi.org/10.1016/j.ocemod.2017.06.010

Neu, U., Akperov, M. G., Bellenbaum, N., Benestad, R., Blender, R., Caballero, R., et al. (2013). Imilast: A community effort to intercompare extratropical cyclone detection and tracking algorithms. *Bulletin of the American Meteorological Society*, *94*(4), 529–547. https://doi.org/10.1175/BAMS-D-11-00154.1

Notz, D., Jahn, A., Holland, M., Hunke, E., Massonnet, F., Stroeve, J., et al. (2016). The CMIP6 Sea-Ice Model Intercomparison Project (SIMIP): Understanding sea ice through climate-model simulations. *Geoscientific Model Development*, *9*(9), 3427–3446. https://doi.org/10.5194/gmd-9-3427-2016

Osbrough, S. L., & Frederiksen, J. S. (2021). Interdecadal changes in Southern Hemisphere winter explosive storms and Southern Australian rainfall. *Climate Dynamics*, *56*(9–10), 3103–3130. https://doi.org/10.1007/s00382-021-05633-y

Papritz, L., Pfahl, S., Rudeva, I., Simmonds, I., Sodemann, H., & Wernli, H. (2014). The role of extratropical cyclones and fronts for Southern Ocean freshwater fluxes. *Journal of Climate*, *27*(16), 6205–6224. https://doi.org/10.1175/JCLI-D-13-00409.1

Perelman, J. N., Tanaka, K. R., Smith, J. N., Barkley, H. C., & Powell, B. S. (2024). Subsurface temperature estimates from a Regional Ocean Modelling System (ROMS) reanalysis provide accurate coral heat stress indices across the Main Hawaiian Islands. *Scientific Reports*, *14*(1), 6620. https://doi.org/10.1038/s41598-024-56865-x

Pfahl, S., & Wernli, H. (2012). Quantifying the relevance of cyclones for precipitation extremes. *Journal of Climate*, *25*(19), 6770–6780. https://doi.org/10.1175/JCLI-D-11-00705.1

Rae, J. G. L., Hewitt, H. T., Keen, A. B., Ridley, J. K., Edwards, J. M., & Harris, C. M. (2014). A sensitivity study of the sea ice simulation in the global coupled climate model, HadGEM3. *Ocean Modelling*, *74*, 60–76. https://doi.org/10.1016/j.ocemod.2013.12.003

Rasch, P. J. (1994). Conservative shape-preserving two-dimensional transport on a spherical reduced grid. *Monthly Weather Review*, *122*(6), 1337–1350. https://doi.org/10.1175/1520-0493(1994)122<1337:CSPTDT>2.0.CO;2

Reale, M., Liberato, M. L. R., Lionello, P., Pinto, J. G., Salon, S., & Ulbrich, S. (2019). A global climatology of explosive cyclones using a multi-tracking approach. *Tellus A: Dynamic Meteorology and Oceanography*, *71*(1), 1611340. https://doi.org/10.1080/16000870.2019.1611340

Reboita, M. S., Da Rocha, R. P., Ambrizzi, T., & Gouveia, C. D. (2015). Trend and teleconnection patterns in the climatology of extratropical cyclones over the Southern Hemisphere. *Climate Dynamics*, *45*(7–8), 1929–1944. https://doi.org/10.1007/s00382-014-2447-3

Rogers, R., Chen, S., Tenerelli, J., & Willoughby, H. (2003). A numerical study of the impact of vertical shear on the distribution of rainfall in Hurricane Bonnie (1998). *Monthly Weather Review*, *131*(8), 1577–1599. https://doi.org/10.1175/2546.1

Ross, R. J., & Kurihara, Y. (1995). A numerical study on influences of Hurricane Gloria (1985) on the environment. *Monthly Weather Review*, *123*(2), 332–346. https://doi.org/10.1175/1520-0493(1995)123<0332:ANSOIO>2.0.CO;2

Saha, S., Moorthi, S., Wu, X., Wang, J., Nadiga, S., Tripp, P., et al. (2014). The NCEP climate Forecast system version 2. *Journal of Climate*, *27*(6), 2185–2208. https://doi.org/10.1175/JCLI-D-12-00823.1

Sanders, F., & Gyakum, J. R. (1980). Synoptic-dynamic climatology of the "Bomb.". *Monthly Weather Review*, *108*(10), 1589–1606. https://doi.org/10.1175/1520-0493(1980)108<1589:SDCOT>2.0.CO;2

Schemm, S. (2018). Regional trends in weather systems help explain Antarctic Sea Ice trends. *Geophysical Research Letters*, *45*(14), 7165–7175. https://doi.org/10.1029/2018GL079109

Schlosser, E., Haumann, F. A., & Raphael, M. N. (2018). Atmospheric influences on the anomalous 2016 Antarctic sea ice decay. *The Cryosphere*, *12*(3), 1103–1119. https://doi.org/10.5194/tc-12-1103-2018

Shchepetkin, A. F., & McWilliams, J. C. (2005). The Regional Oceanic Modeling System (ROMS): A split-explicit, free-surface, topography-following-coordinate oceanic model. *Ocean Modelling*, *9*(4), 347–404. https://doi.org/10.1016/j.ocemod.2004.08.002

Shchepetkin, A. F., & McWilliams, J. C. (2009). Computational Kernel algorithms for fine-scale, multiprocess, longtime oceanic simulations. In *Handbook of numerical analysis* (Vol. 14, pp. 121–183). Elsevier. https://doi.org/10.1016/S1570-8659(08)01202-0

Sinclair, M. R. (1994). An objective cyclone climatology for the southern Hemisphere. *Monthly Weather Review*, *122*(10), 2239–2256. https://doi.org/10.1175/1520-0493(1994)122<2239:AOCCFT>2.0.CO;2

Sinclair, M. R. (1995). A climatology of cyclogenesis for the southern Hemisphere. *Monthly Weather Review*, *123*(6), 1601–1619. https://doi.org/10.1175/1520-0493(1995)123<1601:ACOCFT>2.0.CO;2

Song, Y., & Haidvogel, D. (1994). A semi-implicit ocean circulation model using a generalized topography-following coordinate system. *Journal of Computational Physics*, *115*(1), 228–244. https://doi.org/10.1006/jcph.1994.1189

Steffen, J., & Bourassa, M. (2020). Upper-Ocean response to precipitation forcing in an ocean model hindcast of hurricane Gonzalo. *Journal of Physical Oceanography*, *50*(11), 3219–3234. https://doi.org/10.1175/JPO-D-19-0277.1

Streten, N. A., & Troup, A. J. (1973). A synoptic climatology of satellite observed cloud vortices over the Southern Hemisphere. *Quarterly Journal of the Royal Meteorological Society*, *99*(419), 56–72. https://doi.org/10.1002/qj.49709941906

Thorndike, A. S., Rothrock, D. A., Maykut, G. A., & Colony, R. (1975). The thickness distribution of sea ice. *Journal of Geophysical Research*, *80*(33), 4501–4513. https://doi.org/10.1029/JC080i033p04501

Turner, J., Guarino, M. V., Arnatt, J., Jena, B., Marshall, G. J., Phillips, T., et al. (2020). Recent decrease of summer Sea Ice in the Weddell Sea, Antarctica. *Geophysical Research Letters*, *47*(11), e2020GL087127. https://doi.org/10.1029/2020GL087127

Vichi, M., Eayrs, C., Alberello, A., Bekker, A., Bennetts, L., Holland, D., et al. (2019). Effects of an explosive polar cyclone crossing the Antarctic marginal ice zone. *Geophysical Research Letters*, *46*(11), 5948–5958. https://doi.org/10.1029/2019GL082457

Wang, G., Wu, L., Johnson, N. C., & Ling, Z. (2016). Observed three-dimensional structure of ocean cooling induced by Pacific tropical cyclones. *Geophysical Research Letters*, *43*(14), 7632–7638. https://doi.org/10.1002/2016GL069605

Wang, Y., Rao, Y., Tan, Z.-M., & Schönemann, D. (2015). A statistical analysis of the effects of vertical wind shear on tropical cyclone intensity change over the western North Pacific. *Monthly Weather Review*, *143*(9), 3434–3453. https://doi.org/10.1175/MWR-D-15-0049.1

Warner, J. C., Armstrong, B., He, R., & Zambon, J. B. (2010). Development of a Coupled Ocean–Atmosphere–Wave–Sediment Transport (COAWST) modeling system. *Ocean Modelling*, *35*(3), 230–244. https://doi.org/10.1016/j.ocemod.2010.07.010

Wille, J. D., Alexander, S. P., Amory, C., Baiman, R., Barthélemy, L., Bergstrom, D. M., et al. (2024). The extraordinary march 2022 East Antarctica "heat" wave. Part I: Observations and meteorological drivers. *Journal of Climate*, *37*(3), 757–778. https://doi.org/10.1175/JCLI-D-23-0175.1

Wille, J. D., Alexander, S. P., Amory, C., Baiman, R., Barthélemy, L., Bergstrom, D. M., et al. (2024). The extraordinary March 2022 East Antarctica "heat" wave. Part II: Impacts on the Antarctic ice Sheet. *Journal of Climate*, *37*(3), 779–799. https://doi.org/10.1175/JCLI-D-23-0176.1

Xu, X., Liu, J., & Huang, G. (2022). Understanding Sea surface temperature cooling in the central-East Pacific sector of the southern Ocean During 1982–2020. *Geophysical Research Letters*, *49*(10). https://doi.org/10.1029/2021GL097579

Xu, X., Liu, J., Huang, G., & Ding, Y. (2024). Distribution and trend of explosive cyclones over the Southern Ocean and associated atmospheric and oceanic changes during 1980–2020. *Geoscience Letters*, *11*(1), 38. https://doi.org/10.1186/s40562-024-00356-4

Yang, C., Liu, J., & Xu, S. (2020). Seasonal Arctic Sea Ice prediction using a newly developed fully coupled regional model with the assimilation of satellite Sea Ice observations. *Journal of Advances in Modeling Earth Systems*, *12*(5). https://doi.org/10.1029/2019MS001938

Yang, C.-Y., Liu, J., & Chen, D. (2022). An improved regional coupled modeling system for Arctic sea ice simulation and prediction: A case study for 2018. *Geoscientific Model Development*, *15*(3), 1155–1176. https://doi.org/10.5194/gmd-15-1155-2022

Zhang, J., Lindsay, R., Schweiger, A., & Steele, M. (2013). The impact of an intense summer cyclone on 2012 Arctic sea ice retreat. *Geophysical Research Letters*, *40*(4), 720–726. https://doi.org/10.1002/grl.50190

Zhou, C., Ding, X., Zhang, J., Yang, J., & Ma, Q. (2018). An evaluation of sea surface height assimilation using along-track and gridded products based on the Regional Ocean Modeling System (ROMS) and the four-dimensional variational data assimilation. *Acta Oceanologica Sinica*, *37*(9), 50–58. https://doi.org/10.1007/s13131-018-1225-1